TES Level 1 Algorithms: Interferogram Processing, Geolocation, Radiometric, and Spectral Calibration

Helen Worden, Reinhard Beer, Kevin W. Bowman, Brendan Fisher, Mingzhao Luo, David Rider, Edwin Sarkissian, Denis Tremblay, and Jia Zong

***Abstract*—The Tropospheric Emission Spectromter (TES) on the Earth Observing System (EOS) Aura satellite measures the infrared radiance emitted by the Earth's surface and atmosphere using Fourier transform spectrometry. The measured interferograms are converted into geolocated, calibrated radiance spectra by the L1 (Level 1) processing, and are the inputs to L2 (Level 2) retrievals of atmospheric parameters, such as vertical profiles of trace gas abundance. We describe the algorithmic components of TES Level 1 processing, giving examples of the intermediate results and diagnostics that are necessary for creating TES L1 products. An assessment of noise-equivalent spectral radiance levels and current systematic errors is provided. As an initial validation of our spectral radiances, TES data are compared to the Atmospheric Infrared Sounder (AIRS) (on EOS Aqua), after accounting for spectral resolution differences by applying the AIRS spectral response function to the TES spectra. For the TES L1 nadir data products currently available, the agreement with AIRS is 1 K or better.**

***Index Terms*—Aura, Earth Observing System (EOS), Fourier Transform Spectrometry (FTS), infrared remote sensing, radiometric calibration, Tropospheric Emission Spectrometer (TES).**

I. Introduction

THE Tropospheric Emission Spectrometer (TES) on the Earth Observing System (EOS) Aura platform measures infrared emissions from the Earth's surface and atmosphere [1], [2]. In order to convert the raw measurements into useful radiance spectra, we must perform a series of processing and calibration steps. For an overview of remote sensing using Fourier transform spectrometry, see [3]. The TES L1B Algorithm Theoretical Basis Document (ATBD) V.1.1 [19] is available online for more detailed algorithm descriptions and an updated version, [5], including L1A algorithms will be posted later.

Level 1 (L1) algorithms are separated into Level 1A (L1A), which produces geolocated interferograms and Level 1B (L1B), which produces calibrated spectral radiances. The L1 algorithms have been tested using simulated data as well as real data from the Airborne Emission Spectrometer (AES) [20], and TES pre- and postlaunch calibration tests.

Manuscript received March 8, 2005; revised August 24, 2005. This work was carried out by the Jet Propulsion Laboratory, California Institute of Technology, Pasadena, under a contract with the National Aeronautics and Space Administration.

H. Worden, R. Beer, K. W. Bowman, B. Fisher, M. Luo, D. Rider, E. Sarkissian, and J. Zong are with the Jet Propulsion Laboratory, Pasadena, CA 91109 USA (e-mail: Helen.Worden@jpl.nasa.gov).

D. Tremblay is with Raytheon ITSS, Pasadena, CA 91101 USA.

Digital Object Identifier 10.1109/TGRS.2005.863717

II. L1A Algorithms

A. Interferogram Reconstruction

TES telemetry packets (Level 0 data) comprise three types of data: science, state, and performance. The science packets contain the interferogram measurements. The state packets report instrument status such as temperatures and interferometer and pointing system positions. The performance packets contain more detailed information for the interferometer and pointing systems. Science and state data are generated as part of normal and special measurement sequences, while routine performance data generation is less frequent.

A single interferometer scan creates 64 interferograms associated with the 16 detectors in each of the four focal planes. Scan times are either 4 s for 0.1-cm^{-1} resolution (used for nadir and calibration views) or 16 s for 0.025-cm^{-1} resolution (used for limb views), where values are for apodized resolution. Fig. 1 shows the frequency ranges corresponding to the optical filters used in focal planes designated 2B, 1B, 2A, and 1A. Only one filter may be used per scan per focal plane, but filters can be switched between scans, e.g., for nadir and limb views [1].

Level 0 data records are interleaved and must first be sorted into the channels associated with each TES detector, followed by a mapping to the actual detectors. The index for the interferogram sample that is closest to zero path difference (ZPD) is computed and used later to define the measurement time used for geolocation and further L1B and L2 processing (e.g., see [2] for a complete set of processing level definitions).

L1A processing also converts the state data from $\times$ data numbers (DNs) to the engineering units used for L1B calibration and for monitoring instrument health.

B. Geolocation

L1A geolocation algorithms compute nadir and limb footprint locations (latitude, longitude, and elevation), as well as associated solar and instrument line of sight (LOS) nadir and azimuth angles and Doppler shift.

The nadir footprint, about 8.5 km (along the spacecraft ground track) by 5.3 km (across track), for each 16-detector array, is described by the locations of the four corners of the array. Since TES is a "staring" instrument which compensates for spacecraft motion, there is no change in the footprint over the time of a single nadir measurement. In the limb case, pointing stability allows us to measure at a constant set of altitudes (corresponding to the 16 detectors, each subtending about 2.3 km vertically). However, the volume of air sampled

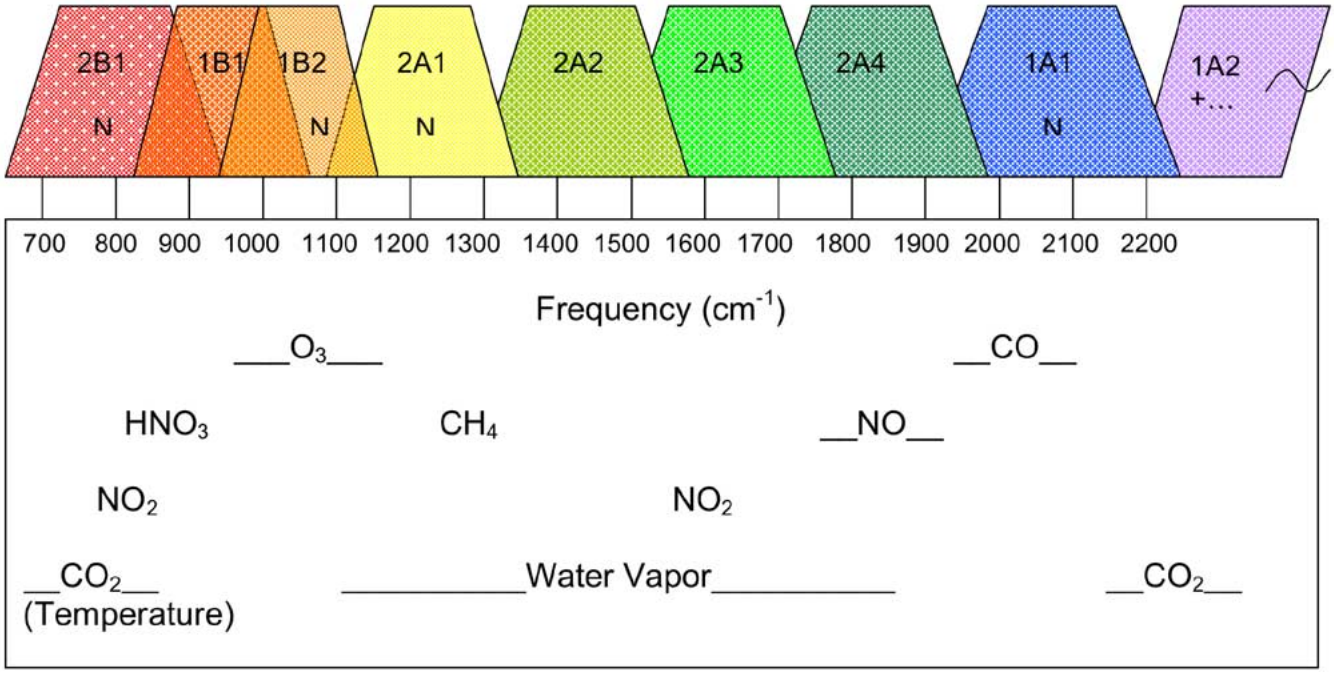

Fig. 1. TES optical filter schematic. Frequency ranges for the optical filters associated with the four 16-detector arrays are shown, with focal planes designated as 2B, 1B, 2A, and 1A. Only one filter can be used per scan per focal plane, but they may be switched between scans. Filters also designated with "N" are those specifically used during the Global Survey for nadir scans. Lines next to molecular species indicate the frequency ranges used in TES standard product retrievals.

does change along the orbit track. The horizontal limb "footprint" is defined as an area extending ± 12 km across track and ± 60 km along track as a consequence of the projected detector geometry and the orbital motion during a scan.

Using the digital elevation model (DEM) with the EGM96 [10] from the EOS Science Data Processing (SDP) Toolkit (see users guide[1]), a mean and standard deviation of heights with respect to the reference geoid are computed for each nadir or limb target footprint. Standard deviations of height for the footprint allow identification of surface relief, such as mountains. These quantities are then used by the L2 retrieval algorithm to compute an average surface pressure. Target scenes with high surface variability are still processed by L2, but may be flagged as "suspect" since only the average surface pressure is used in the radiative transfer forward model.

The geolocation algorithm receives spacecraft attitude and ephemeris data which are combined with the TES pointing control system (PCS) positions to determine target locations. This algorithm also accounts for the internal alignment of the PCS as well as the alignment of TES to the Aura spacecraft.

To estimate geolocation uncertainties we consider two sources: the uncertainty in TES PCS pointing and the reported errors in the spacecraft ephemeris and attitude data. This leads to an estimated geolocation error of about 300 m in the along-track nadir view. Initial evaluation of TES pointing and geolocation has been performed using cloud-free observations over coastlines. The observed gradients in brightness temperatures are consistent with a total geolocation error <1 km. Further validation, using nadir targets such as lakes, with well-characterized, contrasting radiometric features, is being planned.

[1]http://edhs1.gsfc.nasa.gov/waisdata/toc/cd33360001toc.html

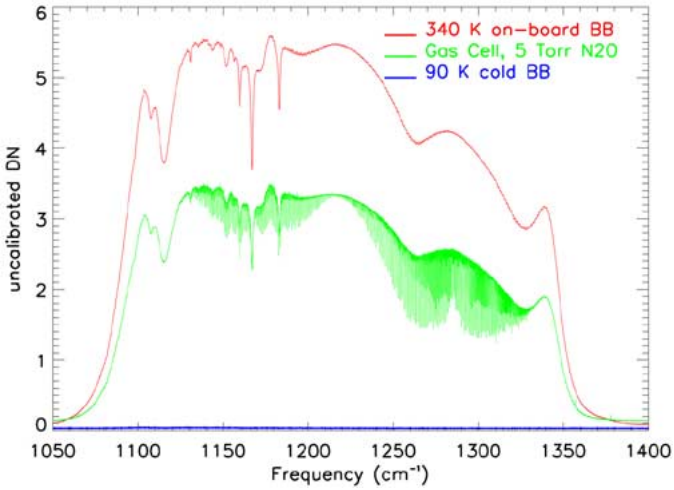

Fig. 2. Examples of target (gas cell) and calibration magnitude spectra from TES ground calibration measurements. Sharp spectral features visible in the 340-K blackbody spectrum are due to a residual hydrocarbon present in the optical path since the instrument was assembled. Since these features are a constant for all calibration and target views, they cancel out in the calibration process.

III. L1B Algorithms

A. Complex Radiometric Calibration

The objective of radiometric calibration is to produce radiance spectra in units of watts per square centimeter per steradian per inverse centimeter ($W/cm^2/sr/cm^{-1}$), with associated estimates of random error called noise equivalent spectral radiance (NESR). The basic algorithm steps for this are as follows:

Step 1) fast Fourier transform (FFT) to spectral space;
Step 2) sampling phase alignment of calibration scans;
Step 3) average and time interpolate calibration scans;

Step 4) perform complex calibration;
Step 5) estimate NESR.

First, we perform an FFT to convert the data from the interferogram domain to the spectral domain. If needed, corrections for detector nonlinearities would be performed on the interferogram before the FFT; however, based on prelaunch testing, these corrections are not necessary (see Section III-C). Although TES measures a "double sided" interferogram, i.e., the scan of optical path goes through ZPD somewhere near the middle, the interferograms are not sampled such that the arrays of measured values are completely symmetric about the point closest to ZPD. Some array padding, with the interferogram mean value, is performed to fill to optimal array sizes. (Array sizes were chosen to have low prime factor values for FFT performance.)

The FFT produces a complex spectrum, $C(\nu)$, where ν is frequency in cm^{-1}, with a phase term defined as

$$\phi(\nu) = \arctan\left(\frac{\mathrm{Im}\,(C(\nu))}{\mathrm{Re}\,(C(\nu))}\right).$$

A perfectly symmetric interferogram would yield a phase of zero. Since TES uses subsampling, combined with optical filters to reduce data rates, a sample point exactly at ZPD is not guaranteed. This sampling offset in interferogram space produces a linear phase term in spectral space. Nonlinear phase terms are also present due to dispersion effects in the optics and electronics.

The technique for performing both phase correction and radiometric calibration, known as "complex calibration," was developed originally for the High-Resolution Interferometer Sounder (HIS) [14] and is now a standard method for calibrating many FTS instruments (e.g., see [18]). This method is preferable to other phase correction techniques, e.g., the FSV method [7], when the phase contribution of the instrument self-emission is nonnegligible or noncolinear with the input radiance, which is the case for TES. The primary assumption is that the instrument phase is stable over the period when calibration and target measurements are acquired. For TES, we apply the following calibration to the complex target spectrum C_{T}, using time interpolated, averaged, complex onboard calibration spectrum C_{BB}, and time interpolated, averaged complex cold-space view spectrum C_{CS}

$$L_{\mathrm{T}} = \frac{C_{\mathrm{T}} - C_{\mathrm{CS}}}{C_{\mathrm{BB}} - C_{\mathrm{CS}}}\varepsilon_{\mathrm{BB}} B(T_{\mathrm{BB}}) \tag{1}$$

where L_{T} is the target radiance in watts per square centimeter per steradian per centimeter, all terms are a function of frequency ν, $\varepsilon_{\mathrm{BB}}$ is the emissivity of the onboard blackbody, and B_{BB} is the Planck function for temperature T_{BB}. Note that the Planck function associated with the cold space view is negligible and that C_{CS} is a measure of the instrument offset radiance. Fig. 2 shows examples of TES ground calibration magnitude spectra representing the measurements for C_{BB}, C_{T}, and C_{CS}, where the target measurement in this case is a gas-cell spectrum. Calibration must be performed separately for each detector and scan direction (i.e., without averaging), since the instrument response is detector and scan direction dependent.

Fig. 3 shows day and night maps (ascending and descending orbit paths, respectively) of observed nadir brightness temperatures computed after radiometric calibration for "window" frequencies near 10 μm. ("Window" frequency ranges are those that have minimal atmospheric absorption.) These maps show the expected behavior for ocean/land and day/night contrasts in brightness temperature, with the exception of low brightness temperatures for cloudy scenes.

Although (1) is straightforward, for TES calibration we must perform a preliminary "sampling phase alignment" step before calibration spectra can be averaged. This is needed because of ambiguity in the starting sample for different scans. The phases of calibration spectra are aligned by adjusting the linear phase term in integer increments corresponding to fringes of the metrology laser. In the global survey mode, TES takes 1152 scans each of the onboard blackbody and cold space. Because of scan direction and filter settings, the number of scans averaged is either a quarter or half of 1152. Therefore, we average 288 spectra for the 1B and 2A arrays since these filters switch between 1B1 and 1B2 and 2A1 and 2A4, respectively, while 576 scans are averaged for the 2B1 and 1A1 filters. This number of averaged scans is more than sufficient to reduce the noise contribution to the calibrated target spectrum to less than 0.5% of the estimated target NESR (at least 16 scans must be averaged for a noise contribution less than 2%).

An important diagnostic from the complex radiometric calibration procedure is the residual signal present in the imaginary spectral terms. The mean values of the imaginary spectra are a good indication of systematic errors since they are due to inaccurate assumptions for phase correction when applying the complex calibration method. Fig. 4 shows an example of the mean imaginary diagnostic for nadir targets in a 16-orbit global survey run for a single detector and filter, for both interferometer scan directions.

The final step in radiometric calibration is to estimate the NESR. If several measurements of the same target (e.g., blackbody sources) are available, the NESR can be estimated by computing the standard deviation of the measurements at each spectral point. In processing however, it is easier to estimate the NESR from single radiance spectra and later compare to the estimate using the standard deviation of several measurements. To estimate the NESR for a single radiance spectrum during complex calibration, we use the RMS of the magnitude of an out-of-band spectral region

$$\mathrm{NESR}(\nu) = \frac{\mathrm{RMS}\,|C_{\mathrm{T}}(\nu_{\mathrm{out\_of\_band}})|}{\sqrt{2}r(\nu)}$$
$$r(\nu) = \frac{|C_{\mathrm{BB}}(\nu) - C_{\mathrm{CS}}(\nu)|}{\varepsilon B(\nu, T_{\mathrm{BB}})} \tag{2}$$

where C_{T} is the single scan complex spectrum, $r(\nu)$ is the instrument response computed using complex averaged calibration spectra C_{BB} and C_{CS}, with Planck function B. Fig. 5 shows examples of the estimated NESR with respect to frequency as well as spectral band averages of NESR with respect to time for the TES 1B2 filter (930 to 1160 cm^{-1}). Representative NESR values for each TES nadir filter are given in Table I.

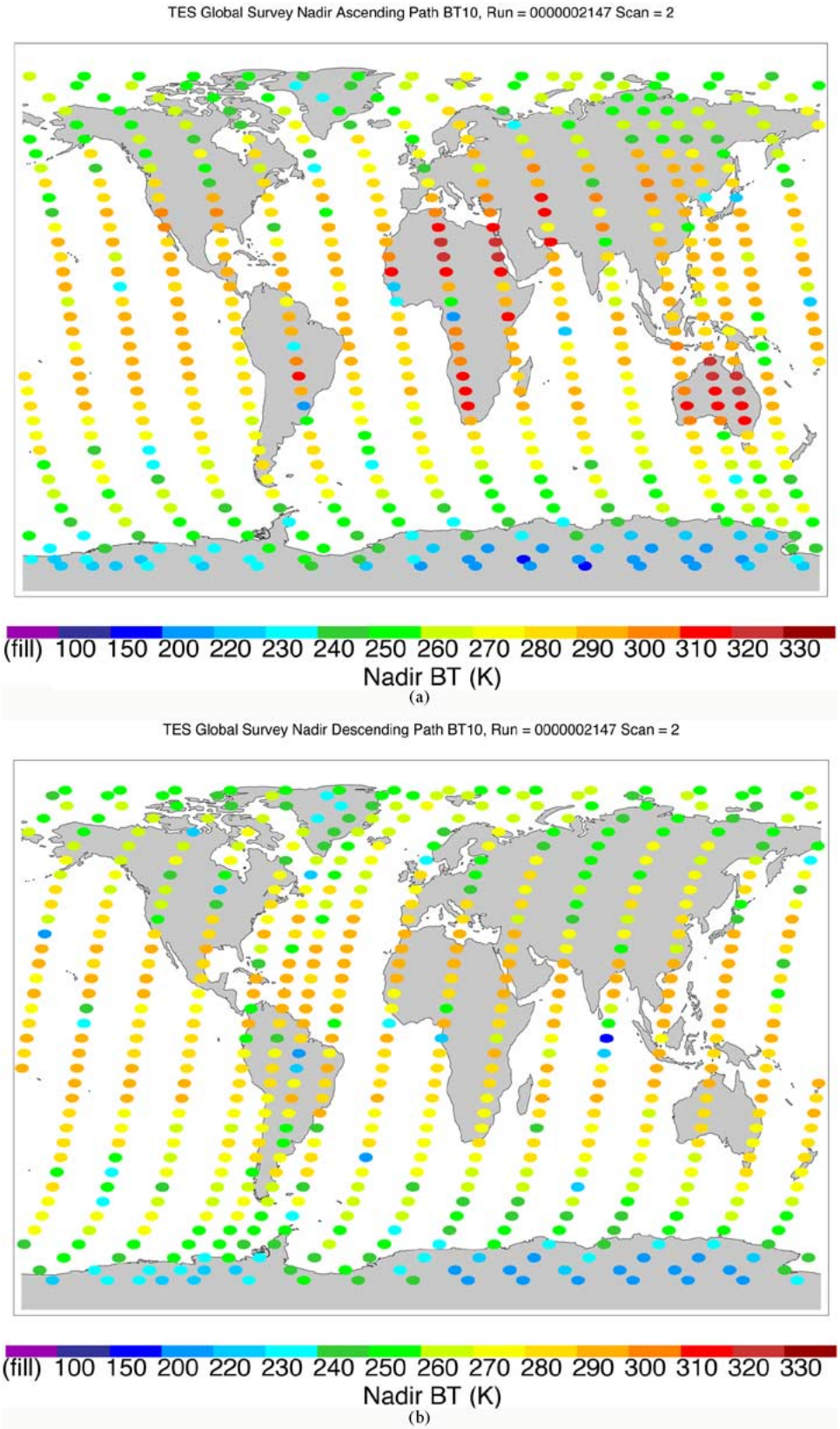

Fig. 3. Maps of TES observed brightness temperatures computed from the 10-μm spectral region for September 20, 2004. The top panel shows the ascending (daytime) portions of the orbits. The bottom panel shows the descending (nighttime) portions. Colors indicate brightness temperature in Kelvin.

B. Spectral Calibration

In order to compute the Planck function used in (1), we must assign a frequency scale for our spectral points. This is done using an updated estimate for the Nd:Yag metrology laser frequency, ν_{laser}, about 9394 cm^{-1}. The laser frequency, although constant for stable operating conditions, can vary with temperature and will need to be calibrated postlaunch and monitored pe-

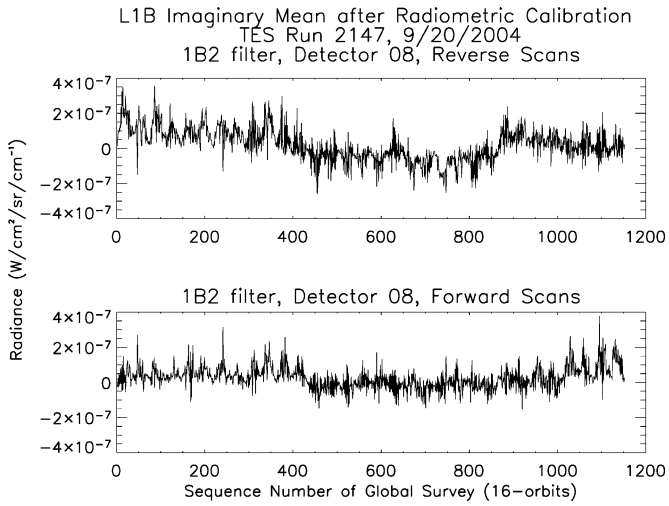

Fig. 4. Examples of imaginary terms, averaged over frequency, after complex radiometric calibration. These terms are a measure of the residual systematic calibration errors present in the reported radiance spectra. The top panel shows the mean imaginary for spectra from interferograms acquired in the reverse scan direction, while the bottom panel shows the same quantity for scans taken in the forward direction. The distinct time and scan direction dependence are being investigated. Additional algorithm development is necessary to mitigate these errors.

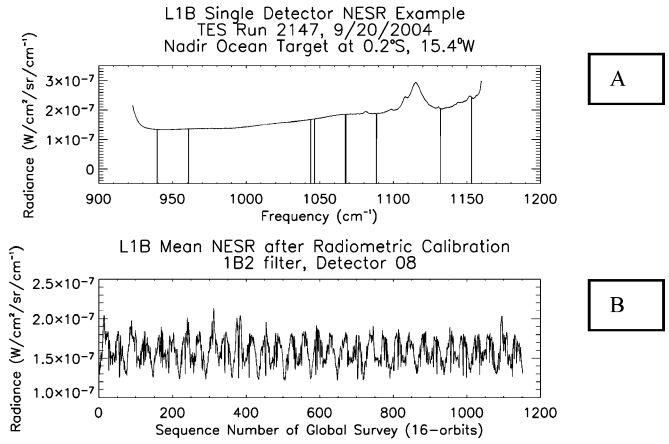

Fig. 5. NESR estimates. Panel A shows the estimated NESR for the TES 1B2 filter, detector 8. Negative values in the NESR indicate the frequency positions of data spikes (unusable spectral values). Panel B shows mean values, averaged over frequency range in panel A, for the NESR estimates over a full 16-orbit Global Survey. A clear orbital variation due to target radiance changes over latitude is present, as expected.

riodically. The minimum frequency $(\nu_{\min})$ and spacing $(\delta\nu)$ for a spectrum of N_{FFT} points measured every N_{step} laser fringes in corresponding alias band N_{alias} are

$$\nu_{\min} = \frac{\nu_{\mathrm{laser}}(N_{\mathrm{alias}} - 1)}{2N_{\mathrm{step}}}; \quad \delta\nu = \frac{\nu_{\mathrm{laser}}}{N_{\mathrm{step}} N_{\mathrm{FFT}}}. \tag{3}$$

To calibrate the laser frequency using TES spectra, we must account for the following:

1) frequency shifts and self-apodization of the instrument line shape (ILS) due to off-axis detectors;
2) Doppler shift (in the case of limb data);
3) resampling to a common frequency grid;
4) model comparison of atmospheric absorption lines.

TABLE I
ERROR ESTIMATES FOR TES NADIR RADIANCE SPECTRA

TES Filter	Freq. Range (cm^{-1})	Syst. Error	Single Detector NESR ($nW/cm^2/sr/cm^{-1}$)	Single Detector NEDT @300 K	Array Average NEDT @300 K
2B1	650-930	2%	700	3.9 K	1.0 K
1B2	920-1160	2%	200	1.3 K	0.3 K
2A1	1090-1350	2%	150	1.2 K	0.3 K
1A1	1890-2260	5%	100	5.5 K	1.5 K

Off-Axis Effects: TES detectors have a $1:10$ aspect ratio and are arranged in rows of 16 per array, along the short dimension as described in [1] and [4]. The interferometer optical axis intersects the array near the middle, but the far pixels have angle >6 mrad away from this axis. The interferogram is therefore an integration over slightly increased optical paths, compared to on-axis, and this results in a frequency compression for an observed monochromatic line. For small angles, this compression is estimated as $\delta\nu(\theta)/\nu_{\theta=0} \approx \theta^2/2$ which is 2×10^{-5} for the highest off-axis angles. In addition to frequency compression, off-axis geometry alters the ILS through "self-apodization" where interferogram amplitudes become attenuated at higher optical path difference (OPD). This results mainly in a wider ILS, i.e., somewhat worse resolution, and is much more significant for higher resolution spectra $(\max.\ \mathrm{OPD} = 33.8\ \mathrm{cm})$ compared to the nominal resolution $(\max.\ \mathrm{OPD} = 8.45\ \mathrm{cm})$. For the nominal resolution and NESR, self-apodization effects were determined to be negligible during ground-based characterization. For high resolution, the effects of self-apodization can be mitigated in L1B as described in [4]. Although L1B data products are unapodized, we note that L2 applies apodization [11] to both measured and model spectra in order to reduce the number of frequencies needed for the forward model calculation.

Doppler Shift: In the TES limb mode, we must account for Doppler shifting of the incoming radiance. Note that this must be done after instrument effects are removed since these are not Doppler shifted. The Doppler shift is computed dynamically for each scan using the velocity reported from the spacecraft telemetry

$$\frac{\delta\nu_{\mathrm{Doppler}}}{\nu} = \frac{\nu_{\mathrm{TES}}}{c} \approx 2.26 \times 10^{-5}.$$

Resampling: Radiance spectra must be resampled to a common frequency grid so they can be averaged (for nadir) and compared to model spectra. This must be done carefully to avoid interpolation errors and computing bottlenecks, as discussed in Sarkissian and Bowman [17]. Using simulated spectra, we estimate the residual errors from self-apodization and resampling to be at the 0.5% level, which is acceptable considering the measurement NESR.

Model Comparison: At this point, the measured frequency positions of atmospheric absorption lines can be compared to the expected model positions. Note that TES does not make

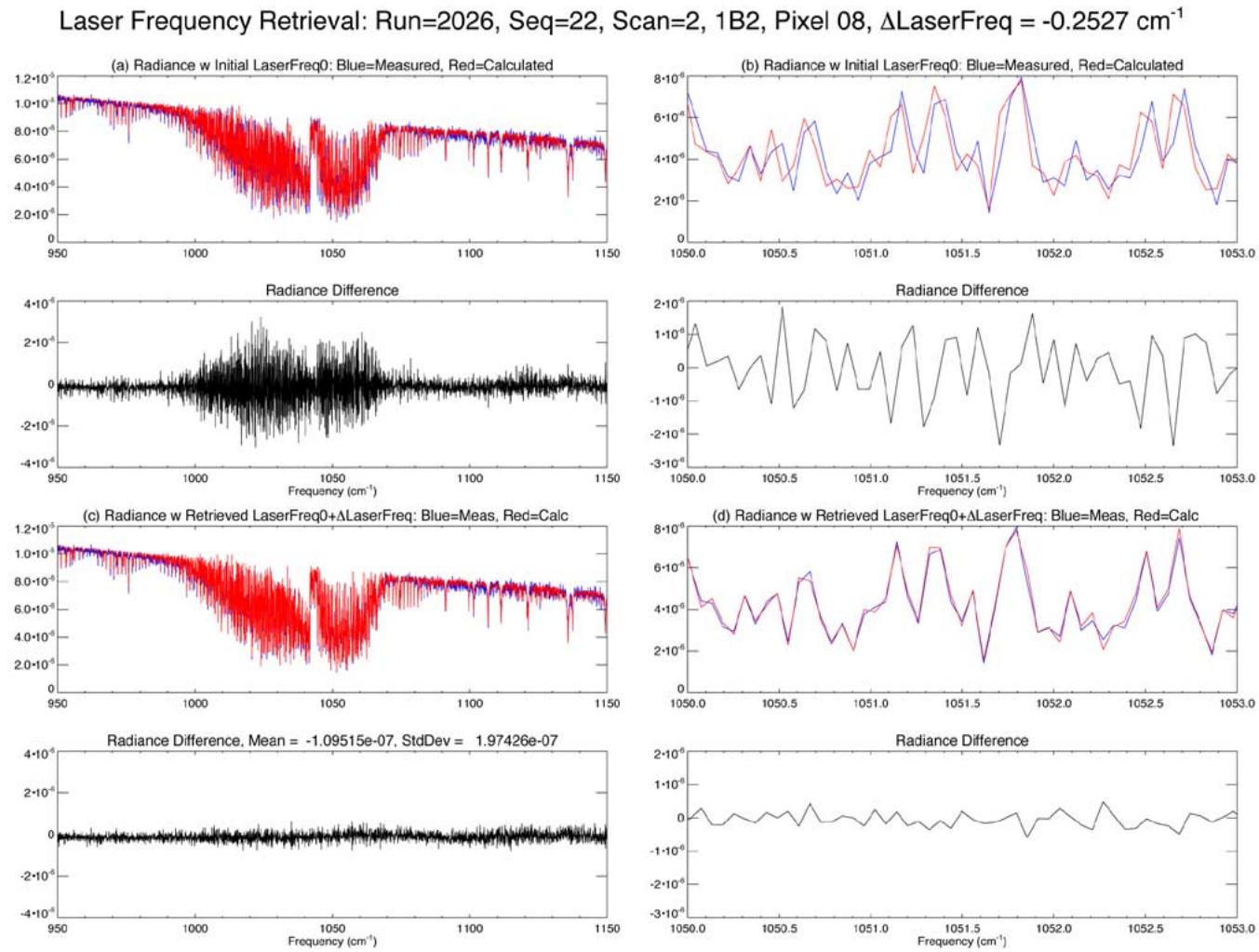

Fig. 6. Example of spectrally calibrated radiance and forward model residuals from TES on-orbit nadir data. Top four panels show the radiance comparison and residual before spectral calibration (right side panels show a zoomed-in frequency range). The bottom four panels show these after spectral calibration.

an absolute frequency determination, but adjusts the laser frequency in (3) as necessary so that measured spectra can be differenced with model spectra in the L2 retrieval. An update to the laser frequency is estimated using a fit to a forward model spectrum [6] based on the HITRAN database [16]. Results of the frequency scale adjustments after fitting for laser frequency only are shown in Fig. 6. A single correction to the laser frequency is sufficient for all wavelengths given that each detector in the four arrays is independently corrected for off-axis frequency compression.

C. Systematic Errors

Sources of systematic errors in TES calibrated radiances include uncertainties in the onboard blackbody temperature, emissivity and view angles, instability in the metrology laser frequency, invalid assumptions about the time variability of the instrument response, offset and phase, and frequency grid interpolation errors.

The TES onboard radiometric calibration source is a cavity blackbody with temperature measured by platinum resistance thermometers (PRT's). The emissivity was modeled using witness sample measurements of the interior coating and was found to be greater than 0.999 below 1700 cm^{-1} and greater than 0.998 above this. Assuming the PRT accuracy and precision (0.1 and 0.01 K, respectively), the systematic brightness temperature error for a 300-K target is 0.08 K, while emissivity errors, if emissivity is assumed to 1.0, are less than 0.06. Compared to noise and other error sources, these are both negligible.

A linear radiance response is implicit in (1) and (2). Since TES detectors are all photovoltaic (PV) HgCdTe, we expect only small nonlinear components to the instrument radiance response. Nonlinearity was characterized at levels below 0.01% during TES ground calibration and should not impact radiometric calibration or atmospheric retrievals.

For the internal view of the onboard blackbody, we assume that: 1) there is no polarization that would introduce an angular dependence of the pointing mirror and 2) a common pointing angle will suffice to fill the detectors in each focal plane. The pointing mirror was designed without overcoating that would produce polarization and none was detected during ground calibration. The common pointing angle assumption was tested both on the ground and on-orbit with results that agree and find the common angle to be slightly less optimal for focal planes 2B and 1B.

The TES metrology laser is temperature controlled for stability. For a typical maximum peak-to-peak temperature variation over a global survey of 0.49 °C, the laser wavelength changes only 0.005 nm. This would not introduce significant time dependence in the spectral phase.

The assumptions we make about time variability in the instrument response and offset are based on our on-orbit calibration spectra and the temperature sensor measurements of different instrument components. A large component of instrument temporal variability is ice build-up on the coldest elements, the detector arrays. Ice absorption has very broad features ($\sim 250\ \mathrm{cm}^{-1}$ FWHM) and is strongest around $830\ \mathrm{cm}^{-1}$, affecting filters 2B1 and 1B1 the most. The detector arrays are periodically heated for decontamination roughly every two months when the integrated signal in 2B1 falls below 50% of the nominal value. This will likely be necessary for the mission lifetime, perhaps with decreased frequency. We also observe the expected latitudinal variability in the instrument thermal environment.

In our current data release, time variability over a global survey is not removed by the calibration and contributes to the systematic errors summarized below. Our prototyping efforts indicate that this source of error is significantly reduced by performing a lease squares estimate of temporal changes in instrument response and offset and applying the corrections to the averaged calibration spectra as they are used to calibrate target data. This allows us to account for time variability while maintaining the same high number of calibration scans used in the calibration averages. We plan to implement this calibration approach, as well as an improved sampling phase alignment algorithm for a future (spring 2006) data release. Residual time variability, on subscan time levels, due to interferogram sampling jitter, is still present, but is only significant near the frequency edges of the optical filters.

Table I summarizes our current estimates for L1B radiance systematic errors and noise levels [NESR and noise-equivalent delta temperature (NEDT)]. These estimates are for nadir targets only and are frequency-band averaged values. The numbers for single detectors are only representative; each detector has unique NESR values. Limb spectral radiance error estimates will be provided in a later publication after further analysis.

IV. Data Quality

Level 1 reports several values and flags related to data quality and processing errors. These can be separated into two types.

1) Target scene quality flags which relate to either cloudy or anomalous scenes that can be flagged using L1B radiances.
2) Data quality flags which relate to instrument and/or processing errors that have either corrupted or degraded the data past the point of being usable in level 2.

Inhomogeneous nadir target scenes, either from viewing broken clouds or a varied surface footprint, are determined by a comparison of brightness temperatures over the 16 detectors of each array. For each TES detector, we calculate average brightness temperatures over specific frequencies in the so-called "window" frequency ranges. These frequency ranges provide the optimal radiance information for the surface or cloud boundary viewed in each target scene. If the variance of brightness temperatures exceeds a threshold determined by the expected noise variance, then the nadir target scene is flagged for high "interpixel variability."

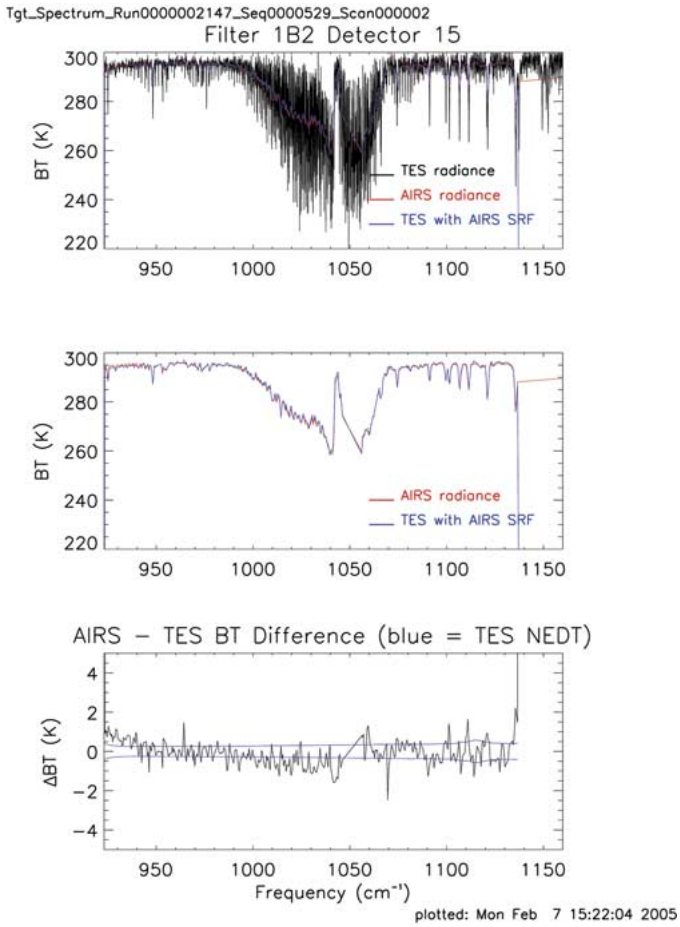

Fig. 7. AIRS-TES comparison of observed brightness temperature spectra from data taken September 20, 2004. Panel A shows a comparison of TES and AIRS nadir brightness temperature (BT) spectra with TES at full spectral resolution. Panel B shows this comparison with the TES spectrum after convolution with the AIRS SRF, and Panel C shows the AIRS-TES brightness temperature difference in brightness with overplotted blue lines indicating the TES noise level at the AIRS spectral resolution, NEDT, in Kelvin.

Data quality flags are set to "bad" when errors such as missing calibration data occur or when quality indicators such as NESR exceed preset thresholds. A complete description of the quality flags is available with TES data products through the Atmospheric Sciences Data Center (ASDC).[2]

V. Radiance Validation

An initial validation of TES radiance spectra was performed by comparing observed nadir brightness temperatures for TES and the Atmospheric Infrared Sounder (AIRS), measured about 12 min apart. AIRS, on the EOS Aqua platform was launched in May 2002 and since then, the AIRS radiance measurements have undergone extensive validation, with reported accuracy at the 0.2-K level for brightness temperatures near 10 μm [9] and [12]. AIRS spectra are taken over circular footprints, each 15 km

[2]http://eosweb.larc.nasa.gov

in diameter while TES detectors have individual footprints of 0.53×5.3 km; 8.5×5.3 km when averaged together. Only observations that are clear over the entire AIRS footprint can be used for comparisons. For quantitative comparisons, the AIRS spectral response function (SRF) [8] and [13] must be applied to TES spectra. An example of the resulting spectra and the difference in brightness temperature between AIRS and TES is shown in Fig. 7, with the estimated NEDT for a TES single detector. Using nadir data from a 16-orbit Global Survey, we find that distributions of AIRS-TES differences in observed brightness temperature for homogenous targets (190 out of 1152 nadir scenes, as determined by TES interpixel variability) have a full-width half-maximum (FWHM) <1 K for the 1B2 spectral range. Although exact radiance comparisons are not possible due to the difference in nadir footprints, this level of agreement with AIRS gives us reasonable initial confidence in our calibrated spectra. Comparisons with AIRS data for homogenous scenes are also used to evaluate improvements with L1B prototype results. Additional radiance validation is being performed using airborne spectra, with finer spatial resolution, from the S-HIS instrument. [15].

VI. Conclusion

We have described the algorithms and diagnostics used to produce the initial TES nadir radiance spectra and NESR. Estimates of the precision (average NESRs) should be valid for current and future data releases but the systematic errors associated with these first products will be updated. Our initial radiance products agree with AIRS spectra to within 1 K and improvements to the calibration algorithms will reduce discrepancies with AIRS to better than 0.5 K.

TES L1 data products are available at the Atmospheric Sciences Data Center (ASDC).[3]

Acknowledgment

This work was performed at the Jet Propulsion Laboratory, California Institute of Technology, under a contract with the National Aeronautics and Space Administration. The TES instrument and continued operation would not be possible without the dedicated efforts of many people. The authors would like to thank the instrument team, the mission operations team and the project management.

References

[1] R. Beer, T. Glavich, and D. Rider, "Tropospheric Emission Spectrometer for the Earth Observing System's Aura satellite," *Appl. Opt.*, vol. 40, pp. 2356–2367, 2001.

[2] R. Beer, "TES on the Aura mission: Scientific objectives, measurements, and analysis overview," *IEEE Trans. Geosci. Remote Sens.*, vol. 44, no. 5, pp. 1102–1105, May 2006.

[3] R. Beer, *Remote Sensing by Fourier Transform Spectrometry*. New York: Wiley, 1992.

[4] K. Bowman, H. Worden, and R. Beer, "Instrument line shape modeling and correction for off axis detectors in Fourier-transform spectrometry," *Appl. Opt.*, vol. 39, 2000.

[5] K. W. Bowman, E. Sarkissian, D. Tremblay, H. Worden, and J. Zong, Tropospheric Emission Spectrometer (TES) Level 1 Algorithm Theoretical Basis Document (ATBD), V. 2.0, JPL, Pasadena, CA, May 2004.

[6] S. A. Clough, M. W. Shepard, J. Worden, P. D. Brown, H. Worden, M. Luo, C. D. Rodgers, C. P. Rinsland, A. Goldman, L. Brown, A. Eldering, S. Sund-Kulawik, K. E. Cady-Pereira, M. C. Lampel, G. Osterman, and R. Beer, "Forward model and Jacobians for Tropospheric Emission Spectrometer retrievals," *IEEE Trans. Geosci. Remote Sens.*, vol. 44, no. 5, pp. 1308–1323, May 2006.

[7] M. L. Forman, W. H. Steel, and G. A. Vanasse, "Correction of asymmetric interferograms obtained in Fourier transform spectroscopy," *J. Opt. Soc. Amer.*, vol. 56, pp. 59–63, 1966.

[8] S. L. Gaiser, H. H. Aumann, L. L. Strow, S. E. Hannon, and M. Weiler, "In-flight spectral calibration of the Atmospheric Infrared Sounder (AIRS)," *IEEE Trans. Geosci. Remote Sens.*, vol. 41, no. 2, pp. 287–297, Feb. 2003.

[9] D. Hagan and P. Minnett, "AIRS radiance validation over ocean from sea surface temperature measurements," *IEEE Trans. Geosci. Remote Sens.*, vol. 41, no. 2, pp. 432–441, Feb. 2003.

[10] F. G. Lemoine *et al.*, The development of the Joint NASA GSFC and NIMA geopotential model EGM96, NASA Goddard Space Flight Center, Greenbelt, MD, 1998.

[11] R. Norton and R. Beer, "New apodizing functions for Fourier spectrometry," *J. Opt. Soc. Amer.*, vol. 66, pp. 259–264, 1976.

[12] T. S. Pagano, H. H. Aumann, D. Hagan, and K. Overoye, "Prelaunch and in-flight radiometric calibration of the Atmospheric Infrared Sounder (AIRS)," *IEEE Trans. Geosci. Remote Sens.*, vol. 41, no. 2, pp. 265–273, Feb. 2003.

[13] L. L. Strow, S. E. Hannon, M. Weiler, K. Overoye, S. L. Gaiser, and H. H. Aumann, "Prelaunch spectral calibration of the Atmospheric Infrared Sounder (AIRS)," *IEEE Trans. Geosci. Remote Sens.*, vol. 41, no. 2, pp. 274–286, Feb. 2003.

[14] H. E. Revercomb, H. Buijs, H. B. Howell, D. D. Laporte, W. L. Smith, and L. A. Sromovsky, "Radiometric calibration of Fourier transform spectrometers: Solution to a problem with the High-Resolution Interferometer Sounder," *Appl. Opt.*, vol. 27, pp. 3210–3218, 1988.

[15] H. Revercomb, R. Knuteson, F. Best, D. Tobin, D. LaPorte, S. Ellington, M. Werner, R. Dedecker, R. Garcia, N. Ciganovich, H. Howell, and W. Smith, "Scanning high-resolution interferometer sounder (S-HIS) aircraft instrument and validation of the Atmospheric InfraRed Sounder (AIRS)," *Fourier Transform Spectrosc.*, vol. 84, pp. 6–9, 2003.

[16] L. S. Rothman, A. Barbe, D. C. Benner, L. R. Brown, C. Camy-Peyret, M. R. Carleer, K. Chance, C. Clerbaux, V. Dana, V. M. Devi, A. Fayt, J.-M. Flaud, R. R. Gamache, A. Goldman, D. Jacquemart, K. W. Jucks, W. J. Lafferty, J.-Y. Mandin, S. T. Massie, V. Nemtchinov, D. A. Newnham, A. Perrin, C. P. Rinsland, J. Schroeder, K. M. Smith, M. A. H. Smith, K. Tang, R. A. Toth, J. Vander Auwera, P. Varanasi, and K. Yoshino, "The HITRAN molecular spectroscopic database: edition of 2000 including updates through 2001," *J. Quant. Spectrosc. Radiat. Transf.*, vol. 82, no. 1–4, pp. 5–44, 2003.

[17] E. Sarkissian and K. W. Bowman, "Application of a nonuniform spectral resampling transform in Fourier-transform spectrometry," *Appl. Opt.*, vol. 42, pp. 1122–1131, 2003.

[18] C. Weddigen, C. E. Blom, and M. Hopfner, "Phase corrections for the emission sounder MIPAS-FT," *Appl. Opt.*, vol. 32, pp. 4586–4589, 1993.

[19] H. M. Worden and K. W. Bowman, Tropospheric Emission Spectrometer (TES) Level 1B Algorithm Theoretical Basis Document (ATBD), V. 1.1, JPL, Pasadena, CA, Oct. 1999. [Online]. Available: http://eospso.gsfc.nasa.gov/atbd/testables.html.

[20] H. M. Worden, R. Beer, and C. P. Rinsland, "Airborne infrared spectroscopy of 1994 western wildfires," *J. Geophys. Res. Atmos.*, vol. 102, no. D1, pp. 1287–1299, 1997.

[3] http://eosweb.larc.nasa.gov

Helen Worden received the Ph.D. degree in particle physics from Cornell University, Ithaca, NY, in 1991.

She is currently a Member of the TES Science Team and works on calibration and retrieval algorithms. She has worked at the Jet Propulsion Laboratory, California Institute of Technology, Pasadena, since 1993.

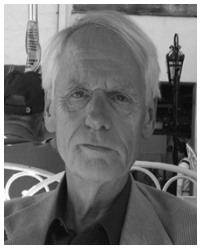

Reinhard Beer received the Ph.D. degree in physics from the University of Manchester, Manchester, U.K., in 1960.

He is currently the Principal Investigator for the Tropospheric Emission Spectrometer on the Earth Observing System Aura satellite launched on July 15, 2004. He joined the Jet Propulsion Laboratory, California Institute of Technology, Pasadena, in 1963.

Kevin W. Bowman received the B.E.E. degree in electrical engineering from Auburn University, Auburn, AL, the Diplôme de Spécialization en Traitement et Transmission des Informations from the Ecole Superieure d'Electricité (SUPELEC), Metz, France, and the M.S. and Ph.D. degrees in electrical engineering from the Georgia Institute of Technology, Atlanta, in 1991, 1992, 1993, and 1997, respectively.

He has been a Member of the Technical Staff at the Jet Propulsion Laboratory, California Institute of Technology, Pasadena, since 1997. His primary research interests are in the area of atmospheric remote sensing and tropospheric chemistry including inverse modeling and data assimilation from satellite observations, estimation and error analysis of trace gas profiles, and calibration algorithms for infrared Fourier transform spectrometers.

Brendan Fisher received the Ph.D. degree in physics from the University of California, San Diego, in 1994.

He is currently a Member of the Science Team for the Tropospheric Emission Spectrometer on the Earth Observing System Aura satellite launched on July 15, 2004. He joined the Jet Propulsion Laboratory, California Institute of Technology, Pasadena, in 1999.

Ming Luo received the Ph.D.degree in atmosphere and space sciences from the University of Michigan, Ann Arbor, in 1991.

She is a member of the Tropospheric Emission Spectrometer (TES) Science Team, Jet Propulsion Laboratory, Pasadena, CA, and works on L2 forward model and retrieval algorithms, data calibration and validation, and L3 algorithms including visualization of TES data.

David Rider received the B.A. degree from Wittenberg University, Springfield, OH, in 1975 and the Ph.D. degree from Michigan State University, East Lansing, in 1975 and 1980, respectively, both in chemistry.

He has been with the Jet Propulsion Laboratory, California Institute of Technology, Pasadena, since 1983, and has served in a variety of roles. He is currently the TES Instrument Scientist.

Edwin Sarkissian received the B.S. degree in computer science and the M.S. degree in applied mathematics from California State University, Los Angeles.

He is currently the Technical Lead for the Level 1B software of the Tropospheric Emission Spectrometer on the Earth Observing System Aura satellite launched on July 15, 2004. He joined the Jet Propulsion Laboratory, California Institute of Technology, Pasadena, in 1995.

Denis Tremblay received the Ph.D. degree in aerospace engineering from the University of Colorado, Boulder, in 1995.

He has been a member of the TES Ground Data System, Raytheon, Pasadena, CA, since 1998. He contributed to the software developement with emphasis on calibration (L1B), geolocation, simulation, integration, testing, and science validation.

Jia Zong received the M.S degree in physics from Southern Illinois University, and the M.S degree in photogrammetry from The Ohio State University, Columbus, in 1989 and 1993, respectively.

She is currently the Cognizant Design Engineer for the Tropospheric Emission Spectrometer Level 1A Geolocation subsystem. She joined the Jet Propulsion Laboratory, California Institute of Technology, Pasadena, in 1994.